Optical grade $(Gd_{0.95-x}Lu_xEu_{0.05})_3Al_5O_{12}$ ceramics with near-zero optical loss: Effects of Lu^{3+} doping on structural feature, microstructure evolution, and far-red luminescence

Zhigang SUN[a], Ji-Guang. LI[b], Huiyu QIAN[a], Yoshio. SAKKA[b], Tohru S. SUZUKI[b], Bin LU[a,c,*]

[a]*School of Materials Science and Chemical Engineering, Ningbo University, Ningbo, Zhejiang 315211, China*

[b]*Research Center for Electronic and Optical Materials, National Institute for Materials Science, Tsukuba, Ibaraki 305-0044, Japan*

[c]*Key Laboratory of Photoelectric Detection Materials and Devices of Zhejiang Province, Ningbo, Zhejiang 315211, China*

* Corresponding author.

E-mail: lvbin@nbu.edu.cn

Abstract: A chemical co-precipitation strategy was employed to synthesize a series of $(Gd_{0.95-x}Lu_xEu_{0.05})_3Al_5O_{12}$ (x = 0.1−0.95) powder phosphors, followed by vacuum sintering to achieve transparent garnet ceramic phosphors. The density functional theory indicated $Lu_3Al_5O_{12}$ was formed in priority compared with $Gd_3Al_5O_{12}$ during solid-phase reaction. Upon high-temperature sintering, the Lu^{3+} substitution for Gd^{3+} suppressed point mass diffusion leading to a smaller grain size. The in-line transmittances of the bulk specimens with x = 0.1, 0.3, 0.5, 0.7, and 0.95 nm were ~83.5, 80.1, 68.8, 73.7, and 82.2% at 710 nm (Eu^{3+} emission center), respectively, among which the x = 0.1 sample exhibited optical grade with near-zero optical loss in agreement with the defect-free single crystal (~100% of the theoretical transmittance). The resulting particle and ceramic materials both presented characteristic Eu^{3+} emission arising from $^5D_0 \rightarrow {}^7F_J$ ($J = 1-4$) transition, where the dominant far-red emission at ~710 nm arising from $^5D_0 \rightarrow {}^7F_4$ transition overlapped with the absorption of phytochrome P_{FR}. The photoluminescence excitation and photoluminescence intensities of $(Gd_{0.95-x}Lu_xEu_{0.05})_3Al_5O_{12}$ powders and ceramics generally increased at a higher Gd^{3+}/Lu^{3+} ratio. Lu^{3+} dopants delayed the fluorescence lifetimes while the bulk samples had shorter lifetimes than the particle counterparts. The transparent $(Gd_{0.85}Lu_{0.1}Eu_{0.05})_3Al_5O_{12}$ ceramic phosphor exhibited good thermal stability with a high thermal quenching temperature above 533 K. The designed ceramic phosphor converted light-emitting diode had a saturation injection current of 435 mA and current-dependent color rendering index. More importantly, our report marked the developmental stage of transparent ceramic materials towards zero optical loss.

Keywords: Transparent ceramics, Garnet, Phosphors, LED, Optical properties, Gibbs free energy

1 Introduction

It is well known that the sunlight plays a crucial role in ecological cycle. In this system, the plants absorb the light energy and then convert the carbon dioxide and water into organic matter with the release of oxygen via photosynthesis. Their light absorption ability derives from the complex and well-defined photoreceptors on plant leaves [1,2]. These photoreceptors have different responses to sunlight, that is, they selectively absorb blue (400−500 nm), red (600−690 nm), and far red (700−740 nm) light regions for phototropic processes, photosynthesis, and photomorphogenesis, respectively [3-5]. Phytochromes are red (P_R)/far-red (P_{FR}) light photoreceptors, which play significant roles in plant growth and development. The phytochrome P_R is biologically inactive upon absorption of red photons into the biological-active P_{FR} state [6]. This is a reversible process, *viz.*, P_{FR} can be also converted back to P_R by absorbing far-red photons. Under far-red light irradiation, the plants would yield shade-avoidance response as if they are blocked from sunlight [7]. Therefore, it is feasible to increase the productivity or adjust the traits of various crops via varying the spectral components (*e.g.*, P_R/P_{FR} ratio) in phytotron chambers or greenhouses [8]. The Mn^{4+} and Cr^{3+} activated luminescent materials can emit far-red light overlapped with the absorption of phytochrome P_{FR}, and thus are frequently used as potential artificial light sources for indoor plant cultivation. A phosphor, if emits multiple beneficial fluorescence signals, may realize the functional diversification for plant cultivation.

Apart from the spectral component, the phosphor material designed as artificial light source for indoor plant cultivation should also have high luminescence efficiency, good luminescent thermal stability, excellent chemical and physical stability, and low cost. The phosphor-converted light-emitting diodes (pc-LEDs) have the advantages over conventional light sources in terms of high luminous efficiency, good durability, low power consumption, compact size, and friendliness to the environment, which make this illuminating system ideal for plant cultivation [9-13]. A ceramic phosphor is superior to the powder counterpart, since the bulk material avoids using the organic polymer as the packaging material which has poor thermal dispersion (thermal conductivity: 0.1−0.4 $W\cdot m^{-1}\cdot K^{-1}$) to readily cause degradation of luminous intensity, acceleration of aging, and changes in emission color upon long-term operation [14]. Besides, the difference in refractive indices between powder phosphor and organic resin would induce light scattering. Hence, the development of transparent ceramic phosphors against using organic resin not only effectively solves these problems but also possesses the merits of more excellent thermal conductivity, optical transmission, chemical stability, luminescent thermal stability, and mechanical property [15].

Body-centered cubic $Ln_3Al_5O_{12}$ (LnAG) aluminates (space group: $Ia\bar{3}d$, No. 230) comprise 160 atoms per unit cell, where the Ln atoms reside in the dodecahedral interstices formed by the corner-sharing arrangement of the AlO_4 and AlO_6 polyhedra [16,17]. In this chemical formula, Lu^{3+}, Y^{3+}, and Gd^{3+} cations are three representative elements for Ln^{3+}. They are attractive host materials owing to their low phonon energy, adjustable bandgap energy, good biocompatibility, and excellent chemical and physical properties. After being doped with rare-earth and/or transition-metal activator(s), these luminescent aluminate materials are extensively applied in the systems of lighting, imaging, laser, optical thermometry, biological sensor, photodynamic therapy, and optical amplifier [18-23]. The Eu^{3+} doped fluorescent material is one of efficient red emission sources arising from 4*f*–4*f* intra-configurational $^5D_0 \rightarrow {}^7F_{1,2}$ transitions [24-28]. However, a Eu^{3+} activated phosphor with strong far-red emission from $^5D_0 \rightarrow {}^7F_4$ transition has relatively rare reports. GdAG:Eu is considered better than YAG:Eu and LuAG:Eu, since a 4*f* energy-level overlap between the ^6P_J state of Gd^{3+} and the ^5H_J state of Eu^{3+} makes energy transfer from Gd^{3+} to Eu^{3+} possible. However, the pure GdAG would suffer from the issue of low thermal stability, namely, GdAG easily decomposes into $GdAlO_3$ perovskite and Al_2O_3 above 1300 °C. Previous reports indicate either substituting Gd^{3+} with smaller Lu^{3+}/Y^{3+} to decrease the average Ln^{3+} radii or replacing Al^{3+} with larger Ga^{3+} to extend the dodecahedral interstices can stabilize the cubic garnet lattice structure [29-31].

The optical loss caused by microdefects in ceramic bodies always exists, leading to an opaque status or a low transparency relative to the corresponding perfect single crystal material. How to achieve a ceramic material with zero optical loss is still a challenge. In the present work, optical grade $(Gd_{0.95-x}Lu_xEu_{0.05})_3Al_5O_{12}$ ceramics were successfully fabricated by cost-effective vacuum sintering. The compositional effects on structure feature, sintering behavior, and optical performance were investigated in detail. Especially, our developed ceramic phosphors exhibit strong far-red and yellow dual emissions for potential application to plant cultivation.

2 Experimental

2.1 Preparation

In a typical synthetic procedure, Gd_2O_3 (~99.999% purity, Haoke Technology Co., Ltd., Beijing, China) and Lu_2O_3 (~99.99% purity, Haoke Technology Co., Ltd., Beijing, China) raw materials are dissolved in excessive hot nitric acid upon heating till dryness to separately prepare the two nitrates.

A mother liquor was obtained by mixing the as-prepared two nitrates, commercial $Eu(NO_3)_3·6H_2O$ (~99.99% purity, Diyang Chemical Co., Ltd., Shanghai, China), and $NH_4Al(SO_4)_2·12H_2O$ (~99.999% purity, Aladdin Biochemical Technology Co., Ltd., Shanghai, China) together according to the chemical formula of $(Gd_{0.95\text{-}x}Lu_xEu_{0.05})_3Al_5O_{12}$ (x = 0–0.95). The molar ratio of Eu^{3+} to total Ln^{3+} cations was fixed at 5 at.%, since above which luminescence quenching would occur [32]. The mother liquor was dripped into a 1.5 M ammonium hydrogen carbonate (AHC, 99.995% purity, Macklin Biochemical Co., Ltd., Shanghai, China) solution at a rate of ~4 mL/min under magnetic stirring at room temperature and the molar ratio of AHC to total cations was kept at 2.5:1. After being aged for 48 h, the suspension was repeatedly washed with distilled water and absolute ethanol via centrifugal separation, followed by drying at 90 ºC for more than 12 h in an oven. The dried precursor was lightly crushed using an agate mortar, and then calcined in a tube furnace under flowing oxygen (~100 mL/min) at 1200 ºC for 4 h to yield the garnet particle. Any additive was not added during the whole particle synthesis process. The powder was pre-compressed in a stainless-steel mold, followed by cold isostatically pressed at 240 MPa. The green body was sintered in a tungsten-heater furnace at 1680–1750 ºC for 4 h under 10^{-4}–10^{-5} Pa vacuum. The sintered body was annealed at 1550 ºC for 7 h in air and was finally polished on both sides to improve surface finish. It should be noted that we selected different temperatures for sintering ceramic samples according to the varying chemical compositions and the specified parameters along with some information on the final sintered products can refer to Table S1 in the the supplementary material.

2.2 Characterization

The as-prepared powders were characterized by X-ray diffraction (XRD; Model D8 Advance Davinci, Bruker, Karlsruhe, Germany) using nickel-filtered Cu$K\alpha$ as incident radiation, Fourier transform infrared spectroscopy (FTIR; Model Nicolet 6700, Thermo, Wisconsin, USA), field emission scanning electron microscopy (FE-SEM; Model S-4800, Hitachi, Tokyo, Japan), and laser diffraction particle size analyzer (Model Nano-ZS90, Malvern Instruments, Malvern, UK). The in-line transmittances of polished ceramics were measured on a UV/VIS/NIR spectrophotometer (Model Lambda 950, Perkin-Elmer, Massachusetts, USA) from 200 to 2100 nm. The microstructures of the bulks were observed on a desktop scanning electron microscope (D-SEM; Model EM-30plus, COXEM, Daejeon, Korea). The photoluminescence (PL), photoluminescence excitation (PLE), and fluorescence decay kinetics of phosphors and ceramics were recorded on two different steady-state fluorescence spectrometers, that is, the Model FS5 equipment (Edinburgh Instruments, Edinburgh, UK) for spectral test and the Model FLS 980 one (Edinburgh Instruments) for decay behavior measurement. The quantum efficiency was determined by a professional quantum efficiency measurement system (Model QE-2100, Otsuka Electronics, Shiga, Japan). The electroluminescence (EL) spectra of the assembled LED device at diverse forward bias currents were measured using a multi-channel spectroradiometer (Model SPEC 3000A, Measurefine Instrument, Hangzhou, China).

2.3 Computational methodology

First-principles calculations are performed in the framework of the density functional theory (DFT) with the projector augmented plane-wave method, as implemented in the Vienna ab initio simulation package. The generalized gradient approximation proposed by Perdew, Burke, and Ernzerhof is selected for the exchange-correlation potential [32]. The calculations are done on the two chemical compositions of $Lu_3Al_5O_{12}$ and $Gd_3Al_5O_{12}$. The cut-off energy for plane wave is set to 450 eV. The energy criterion is set to 10^{-5} eV in iterative solution of the Kohn-Sham equation. The Brillouin zone integration is performed using a 6×6×6 k-mesh. All the structures are relaxed until the residual forces on the atoms have declined to less than 0.01 eV/Å.

3 Results and discussion

3. 1 Density functional theory

$$3Gd_2O_3(s) + 5Al_2O_3(s) = 2Gd_3Al_5O_{12}(s) \tag{1}$$

$$3Lu_2O_3(s) + 5Al_2O_3(s) = 2Lu_3Al_5O_{12}(s) \tag{2}$$

Equations (1) and (2) are two crucial reactions during the whole particle synthesis process. Current database lacks related thermodynamic functions for the two products of $Gd_3Al_5O_{12}$ and $Lu_3Al_5O_{12}$, and thus DFT is used for calculation. DFT-optimized configuration for $Gd_3Al_5O_{12}$ or $Lu_3Al_5O_{12}$ contains 65 atoms. In the standard state (101325 Pa), the changes in the Gibbs free energies (Δ*G*) for Eqs. (1) and (2) at 1200 ºC are respectively determined to be -4.28 and -4.46 eV/atom based on the algorithm as denoted in Eq. (3) [33].

$$\Delta G(T,P) = G_{Ln_3Al_5O_{12}}(T,P) - [G_{Ln_2O_3}(T,P) + G_{Al_2O_3}(T,P)] - \Delta H_f(T,P) \qquad (3)$$

3. 2 Structural features of synthetic products

Our co-precipitation method leads to rounded precipitation precursors with frequently empty interiors upon pyrolysis into relatively discrete rounded garnet powders without observed hard agglomeration (Fig. S1 in the supplementary material). Those precursors are primary in amorphous states (Fig. S2 in the supplementary material). The chemical compositions of precipitation precursors are qualitatively analyzed by FTIR spectra and the results reveal that the precursors possess the structure of hydrated basic carbonate sulfate (Fig. S3 in the supplementary material).

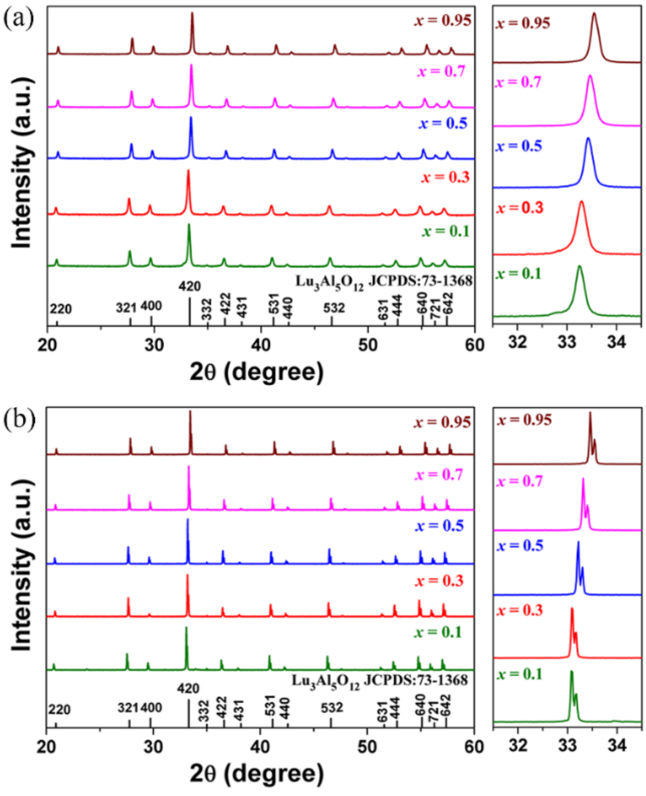

Fig. 1 XRD patterns of the target particle products for $(Gd_{0.95-x}Lu_xEu_{0.05})_3Al_5O_{12}$ (x = 0.1−0.95) obtained by calcining the precursors at 1200 ºC for 4 h (a) and the corresponding bulk materials fabricated by vacuum sintering (b). The two insets in the right-hand panels show the enlarged view of the main (420) diffraction peak.

Figure 1(a) exhibits the XRD patterns of target particle products for $(Gd_{0.95-x}Lu_xEu_{0.05})_3Al_5O_{12}$ (x = 0.1−0.95) obtained by calcining the precursors at 1200 ºC for 4 h. Their XRD peaks can be well indexed into the cubic $Lu_3Al_5O_{12}$ standard card (JCPDS No. 73-1368) without observed other impure phase, indicating that the precipitation precursors have completely transformed into pure garnet phase via thermal decomposition. TG analysis further reveals that the pyrolytic processes include dehydroxylation, dehydroxylization, decarbonation, desulfuration, and solid-phase reaction (Fig. S4 in the supplementary material), while a higher Gd^{3+}/Lu^{3+} ratio leads to a higher decomposition temperature on each stage due to the higher alkalinity of Gd^{3+} than that of Lu^{3+}. The crystallite size (D_{XRD}) can be calculated from the full width at half maximum (FWHM) of the (420) diffraction band using Scherrer's equation: $D_{XRD} = K\lambda/(\beta Cos\theta)$, where K is the shape factor (K = 0.89), λ is the wavelength of X-ray (λ = 0.15406 nm), β is the FWHM, and θ is the Bragg angle [34-37]. The determined crystallite sizes are ~135, 123, 122, 116, and 97 nm for the specimens with x = 0.1, 0.3, 0.5, 0.7, and 0.95, respectively. The reduced crystallite size with more Lu^{3+} doping is associated with thermodynamics. The whole calcination processes include thermal decomposition and solid-phase reaction. A high-temperature solid-phase reaction primarily comprises chemical reaction and diffusion process, where the chemical reaction is generally faster than the diffusion process for most of solid-phase reaction. On the other hand, the crystallite formation mainly includes nucleation and growth. Therefore, a chemical reaction that is more prone to occur will provide more nuclei, and vice versa. The ΔG value of Eq. (2) is smaller than that of Eq. (1), suggesting that $Lu_3Al_5O_{12}$ is formed in priority during high-temperature solid-phase reaction, and thus a higher Lu^{3+}/Gd^{3+} ratio would create more crystal nuclei to reduce the average crystallite size.

After vacuum sintering, all ceramic samples still maintain the cubic garnet structure [Fig.1(b)]. For the purposes of better comparison, we also prepare a ceramic composition according to $Gd_3Al_5O_{12}$. After sintering at 1650 ℃, this specimen exhibits main orthorhombic perovskite structure with a small number of Al_2O_3 phase due to the thermal decomposition behavior: $Gd_3Al_5O_{12} \rightarrow 3GdAlO_3 + \alpha\text{-}Al_2O_3$ at a high temperature (Fig. S5 in the supplementary material). Therefore, more than 10 at.% Lu^{3+} substitution for Gd^{3+} has been proved to be effective enough for stabilizing the cubic GdAG phase structure via reducing the average Ln^{3+} radius. The XRD patterns of ceramics become much sharper relative to those of powders. Additionally, the (420) diffraction bands of bulk specimens are slightly splitting in accordance with that of $Lu_3Al_5O_{12}$ single crystal [38,39], but the powder samples exhibit symmetrical peak profiles. These phenomena both indicate that the crystallinity of the ceramic materials has been greatly improved via grain growth at high temperatures. It can be obviously noted that the (420) diffraction peaks of the garnet powders and ceramics both shifts towards the high angle side with increasing Lu^{3+} incorporation. This is because the decreasing average ionic radius of Ln^{3+} induces the continuous shrinkage of the unit cell with the increase in the amount of Lu^{3+} substitution for Gd^{3+}, which also confirms that the Lu^{3+} and Eu^{3+} dopants have been substantially dissolved into the GdAG lattice.

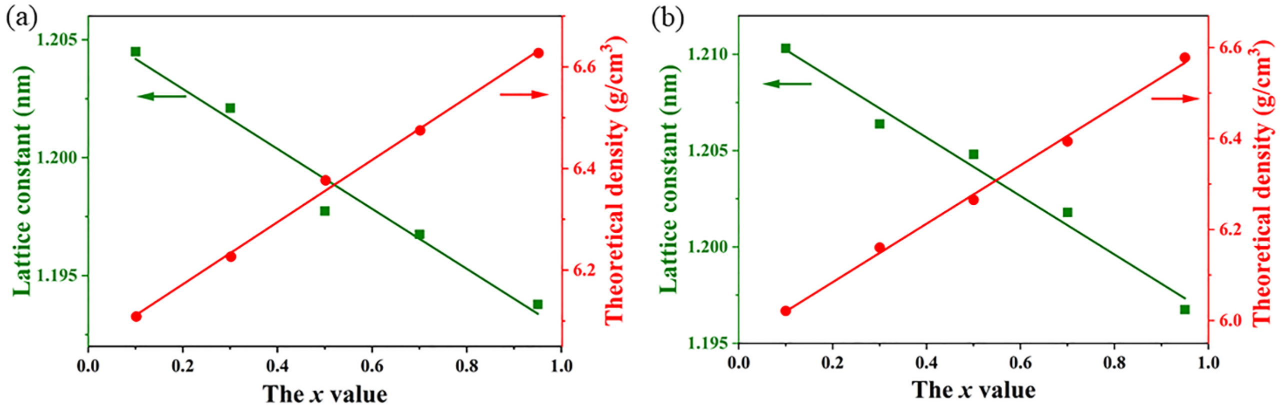

Fig. 2 Lattice constants and theoretical densities of $(Gd_{0.95\text{-}x}Lu_xEu_{0.05})_3Al_5O_{12}$ powders (a) and ceramics (b) as a function of *x* value.

Figure 2 shows the lattice constants and the theoretical densities of $(Gd_{0.95\text{-}x}Lu_xEu_{0.05})_3Al_5O_{12}$ powders and ceramics as a function of Lu^{3+} content. The lattice constants are calculated according to XRD data using Bragg's equation. Their lattice constants almost linearly decrease at a higher Lu^{3+} concentration. Such a phenomenon complies with Vegard's law [40], suggesting that homogeneous garnet solid solutions have formed. It should be noted that the powder material has a smaller cell parameter than the bulk counterpart at each Lu^{3+} concentration. From bulks to nanocrystallites, the lattice expansion or contraction phenomena are both possibly observed according to previous reports [41,42], where the former is caused by internal stress and latter is due to surface tension. Herein, our case belongs to surface tension. The theoretical densities (d_{th}) of these solid solutions can be determined from Eq. (4):

$$d_{th} = \frac{8}{a^3 N_A}\{[mM_{Lu} + nM_{Eu} + (1-m-n)M_{Gd}]\times 3 + 5M_{Al} + 12M_O\} \tag{4}$$

where a represents for the lattice constant, M_i stands for the atomic weight of element i (i = Lu, Gd, Eu, and O), N_A denotes the Avogadro constant, and m and n refer to the atomic percentages of Lu^{3+} and Eu^{3+}, respectively [43]. Their theoretical densities linearly rise with the increase in Lu^{3+} content due to the heavier Lu^{3+} than Gd^{3+}, namely, gradually approaching the theoretical density of $Lu_3Al_5O_{12}$ (6.67−6.73 g/cm^3) [44,45].

3.3 Transmittances and microstructures of $(Gd,Lu)_3Al_5O_{12}$:Eu ceramics

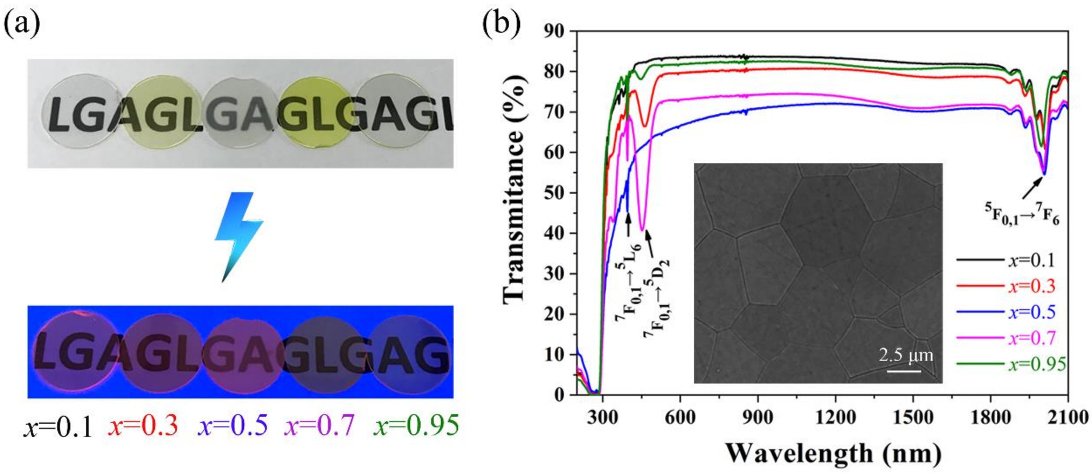

Fig. 3 Appearances (a) and in-line transmittances (b) of transparent $(Gd_{0.95-x}Lu_xEu_{0.05})_3Al_5O_{12}$ (x = 0.1−0.95) ceramics. The lower part in panel (a) shows the red emission of $(Gd,Lu)_3Al_5O_{12}$:Eu ceramics irradiated by a 365 nm ultraviolet lamp. The embedded image in panel (b) displays the thermal etching polished surface of the best specimen with x = 0.1. The samples are all ~1.0 mm in thickness.

The appearances and in-line transmittances of vacuum sintered $(Gd_{0.95-x}Lu_xEu_{0.05})_3Al_5O_{12}$ (x = 0.1−0.95) ceramics are shown in Fig. 3. The letters under the five ceramics are able to be well read-through upon 365 nm ultraviolet lamp irradiation into characteristic orange emission of Eu^{3+} [Fig. 3(a)]. Nevertheless, the orange emission seems not strong to the naked eyes. This is because the most intense excitation band of Eu^{3+} locates at 394 nm rather than 365 nm [Fig. 5(c)]. Another reason is that the dominant $^5D_0\rightarrow{}^7F_4$ emission of Eu^{3+} locates at ~710 nm [Fig. 5(d)], whilst the human eye sensitivity greatly decreases at 650 nm and approaches almost nil at 700 nm. In natural light, the two specimens with x = 0.3 and 0.7 exhibit yellowish hue, whereas the other three samples are normally colorless. The color is closely associated with the transmission behaviors. As indicated in Fig. 3(b), the absorption peaks in the transmittance curves are caused by intra-$4f^6$ transitions of Eu^{3+}, but the x = 0.3 and 0.7 samples have stronger absorption extent around 455 nm blue region and thus appear the optical compensatory yellow color. Such a phenomenon may be related to more oxygen defects. Under vacuum sintering at elevated temperature, the oxygen vacancy is easy to form while an extra defect energy level may be introduced. This new energy level may be around $^5D_2$ state of Eu^{3+} to enhance $^7F_{0,1}\rightarrow{}^5D_2$ absorption. It should be noted that these oxygen vacancies induced under oxygen deficient condition are unstable, and also difficult to be precisely controlled. Even if the ceramics are treated by post-annealing, the oxygen in air is not always able to fully fill up in the vacancy site via diffusion in the dense sintered body.

The in-line transmittances of ceramic specimens with x = 0.1, 0.3, 0.5, 0.7, and 0.95 are ~83.5, 80.1, 68.8, 73.7, and 82.2% at 710 nm (Eu^{3+} emission center), respectively, among which the 10 at.% Lu^{3+}-stabilized GdAG:Eu bulk sample has the best optical quality. The theoretical transmittance (*T*) for a defect-free $Lu_3Al_5O_{12}$ single crystal can be deduced from the relationship between refractive index (*n*) and wavelength (λ) as follows [Eqs. (5)−(7)]:

$$T = (1-R)^2 exp(-\alpha t) \tag{5}$$

$$R = \frac{(n-1)^2}{(n+1)^2} \tag{6}$$

$$n^2 = 1 + \frac{\lambda^2}{0.4335\lambda^2 - 0.0055} \tag{7}$$

where α is the loss factor and t is the sample thickness [46-48]. Assuming α = 0, the calculated refractive index and theoretical transmittance at 710 nm are ~1.83 and ~83.5%, respectively, and hence the corresponding ceramic specimens with x = 0.1, 0.3, 0.5, 0.7, and 0.95 are equivalent to ~100, 96, 82, 88, and 98% of the theoretical value. Even more importantly, the x = 0.1 sample exhibits optical grade with near-zero optical loss in accordance with the defect-free single crystal. Such an almost perfect optical quality has a scarce report for any transparent ceramic material, further revealing the advancement of our ceramic technology.

The thermal etching microstructure of the best x = 0.1 sample is shown in the inset of Fig. 3(b). Its statistic average grain size via WinRoof image analysis software is only around 7.5 μm. The quite fine grain size contributes to improved mechanical property. Additionally, the grain size is relatively uniform, and no abnormal grain growth or residual pores can be observed. The relative density of the ceramic is determined to be ~100% by Archimedes method, in agreement with the pore-free dense structure and the excellent optical quality.

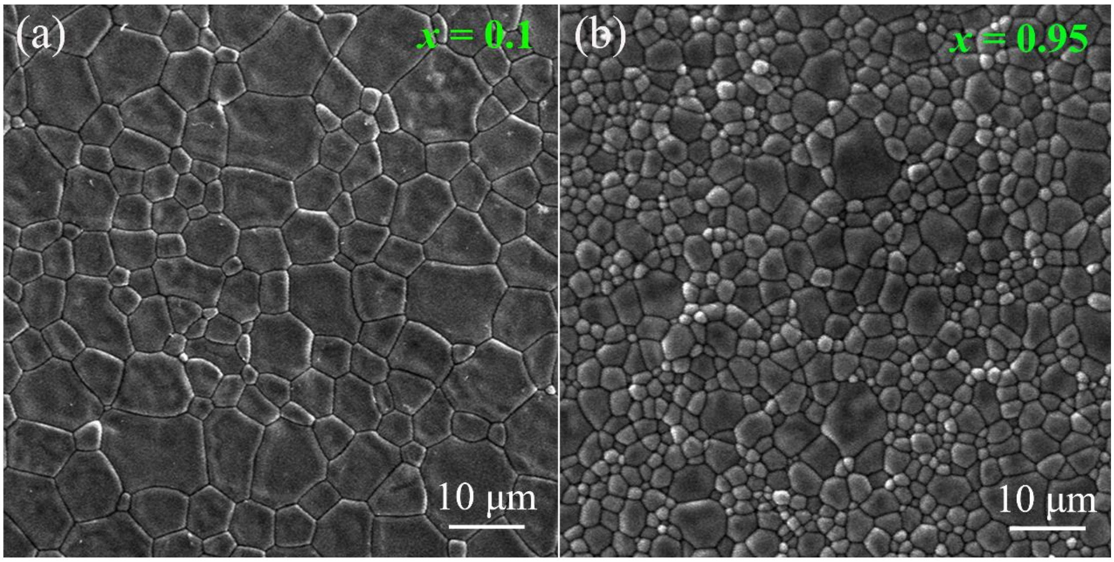

Fig. 4 D-SEM micrographs showing the surface microstructures of vacuum sintered $(Gd_{0.95-x}Lu_xEu_{0.05})_3Al_5O_{12}$ specimens with $x = 0.1$ (a) and 0.95 (b).

Figure 4 compares the surface microstructures of $(Gd_{0.95-x}Lu_xEu_{0.05})_3Al_5O_{12}$ ceramic specimens with $x = 0.1$ and 0.95, which are sintered at an identical temperature of 1680 ºC. Their average grain sizes are counted to be ~9.8 μm for $x = 0.1$ and ~2.5 μm for $x = 0.95$. Apparently, the former has a larger grain size than the latter. Point mass diffusion, such as grain-boundary diffusion and volume diffusion, mainly determines the grain size. The more Gd^{3+}/Lu^{3+} ratio in the garnet system leads to faster point mass diffusion, which is somewhat similar to our previously reported $(Y,Gd)_2O_3$-based sesquioxide [49]. Considering that the particle crystallite size originally decreases with increasing Lu^{3+} addition (Fig. 1), these phenomena imply that the crystallites in powders may undergo nearly synchronous growth upon subsequent sintering densification. It should be noted that the same bulk sample (e.g. $x = 0.1$) has discrepant statistic average grain sizes from the thermal etching polished surface [~7.5 μm in the inset of Fig. 3(b)] and untreated surface [~9.8 μm in Fig. 4(a)]. Apparently, the latter is larger than the former because of the preferential sintering on surface. In practice, the statistic value on the thermal etching polished surface has better representativeness.

3.4 Spectral behaviors of the phosphor particles and ceramics

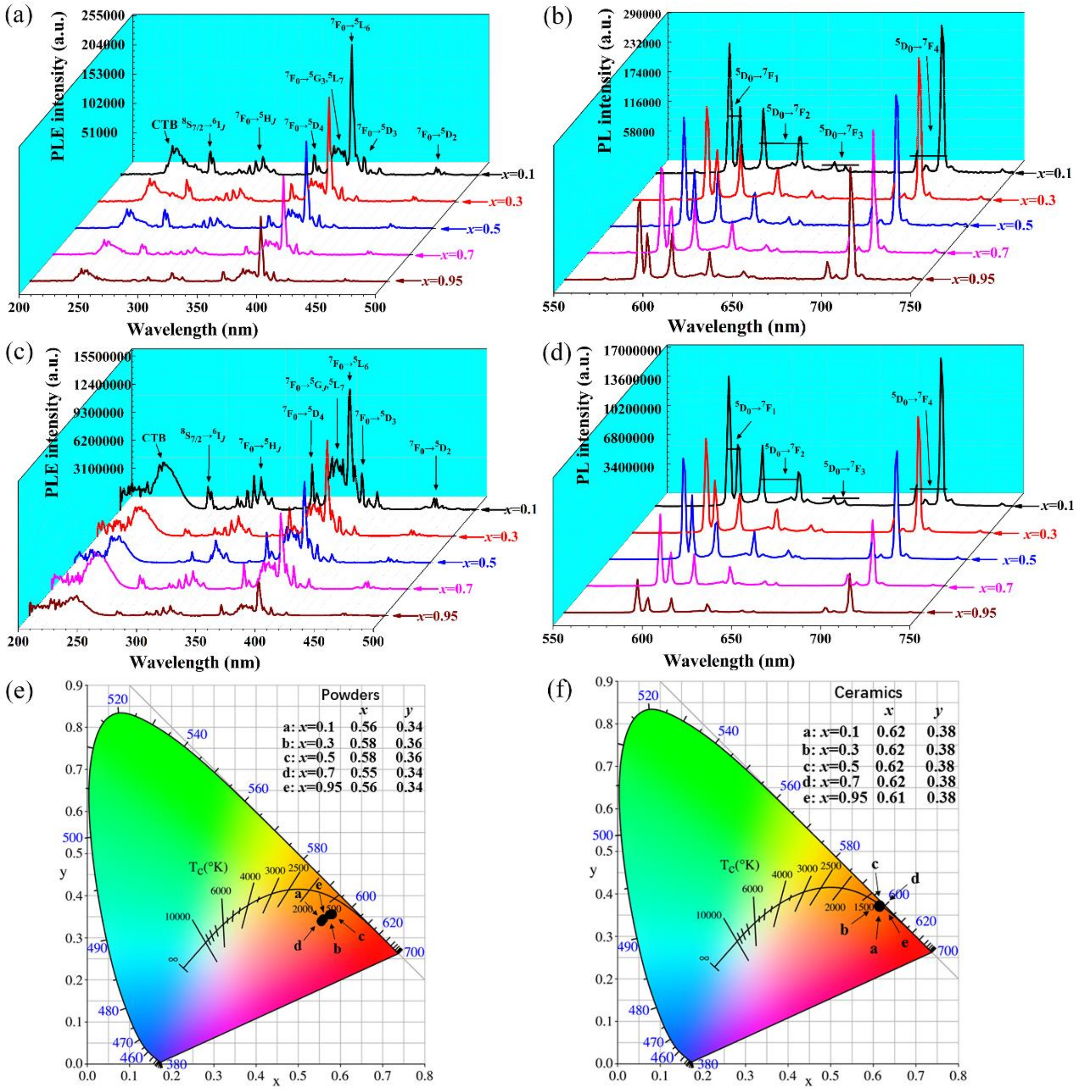

Fig. 5 PLE (a, c) / PL spectra (b, d) and CIE chromaticity diagrams (e, f) of $(Gd_{0.95-x}Lu_xEu_{0.05})_3Al_5O_{12}$ powders (a, c, e) and ceramics (b, d, f) as a function of *x* value.

Figure 5(a) presents the PLE spectra of $(Gd_{0.95-x}Lu_xEu_{0.05})_3Al_5O_{12}$ (x = 0.1−0.95) powders as a function of Lu^{3+} concentration. The broad band at ~230–267 nm is caused by charge transfer (CT) from the 2*p* orbital of O^{2-} to the 4*f* orbital of Eu^{3+} and the neighboring peak at ~275 nm is attributed to the $^8S_{7/2}\rightarrow{}^6I_J$ transition of Gd^{3+} [49,50]. The other weak excitation peaks beyond 300 nm are assignable to intra-$4f^6$ transition of Eu^{3+} as indicated in Fig. 5(a), among which the strongest one locates at ~394 nm arising from $^7F_0\rightarrow{}^5L_6$ transition of Eu^{3+}. Under 394 nm excitation, the corresponding PL spectra exhibit characteristic Eu^{3+} emissions deriving form $^5D_0\rightarrow{}^7F_J$ (J = 1−4) transitions, where the $^5D_0\rightarrow{}^7F_1$ transition at ~592−596 nm belongs to magnetic-dipole transfer, the $^5D_0\rightarrow{}^7F_{2,4}$ transitions (~610−630 nm for $^5D_0\rightarrow{}^7F_2$ transition and ~696−710 nm for $^5D_0\rightarrow{}^7F_4$ transition) ascribe to electric-dipole transfer, and the $^5D_0\rightarrow{}^7F_3$ transition at ~650−656 nm is forbidden [25]. Thereinto, the $^5D_0\rightarrow{}^7F_4$ emission dominates in each case. The $^5D_0\rightarrow{}^7F_0$ transition of Eu^{3+} (generally at ~580 nm) is absent because it only exists in the point symmetric C_s, C_n, and C_{nv} (n = 1, 2, 3, 4, 6) sites [51]. However, a cubic garnet lattice provides a crystallographic D_2 position for Eu^{3+} substitution. The D_2 lattice site has a high degree of symmetry, but Eu^{3+} ions sometimes reside at the deviation site of dodecahedral interstices. As a result, either the magnetic-dipole $^5D_0\rightarrow{}^7F_1$ transition or the electric-dipole $^5D_0\rightarrow{}^7F_4$ transfer likely dominates in the emission spectra of Eu^{3+} doped garnet systems, while their ratio depends on not only the surrounding environment but also the cationic average electronegativity [52]. In this work, the electric-dipole $^5D_0\rightarrow{}^7F_4$ transition presents the strongest intensity due to the geometric distortion.

The PLE and PL spectra of $(Gd_{0.95-x}Lu_xEu_{0.05})_3Al_5O_{12}$ ceramics are shown in Figs. 5(c) and (d). The band positions of ceramics basically have no change relative to those of powders, but the PLE and PL intensities significantly increase. By taking x = 0.1 sample as an example, the ceramic phosphor exhibits ~20.5-fold higher PL intensity than the particle counterpart. Additionally, the PLE/PL intensities of $(Gd_{0.95-x}Lu_xEu_{0.05})_3Al_5O_{12}$ powders and ceramics gradually rise at a higher Gd^{3+}/Lu^{3+} ratio, where the specimen with x = 0.1 has the strongest intensity (~3.8 times that of the counterpart with x = 0.95). The enhanced luminescence cannot ascribe to the energy transfer from Gd^{3+} to Eu^{3+}, because the 394 nm excitation wavelength (~3.1 eV) is not enough to excite the electrons of the ground state onto the ^6P_J level of Gd^{3+} (~4.0−4.1 eV) as illustrated in Fig. S6 of the supplementary material. The reason can consider the average electronegativity for Ln^{3+}. That is, Gd^{3+} is less electronegative than Lu^{3+} (1.20 for Gd^{3+} and 1.27 for Lu^{3+}), and thus a higher Gd^{3+}/Lu^{3+} ratio facilitates electron transfer. By comprehensively considering the spectral behaviors as well as the optical transmittances, the optimum ceramic composition is $(Gd_{0.85}Lu_{0.1}Eu_{0.05})_3Al_5O_{12}$.

The Commission International de I'Eclairage (CIE) chromaticity diagrams of $(Gd_{0.95-x}Lu_xEu_{0.05})_3Al_5O_{12}$ phosphors and ceramics under 394 nm excitation are drawn in Figs. 5(e) and (f). The CIE chromaticity coordinates of $(Gd_{0.95-x}Lu_xEu_{0.05})_3Al_5O_{12}$ powders are (0.56, 0.34), (0.58, 0.36), (0.58, 0.36), (0.55, 0.34), and (0.56, 0.34) for the specimens with x = 0.1, 0.3, 0.5, 0.7, and 0.95, respectively, which all lie in the yellowish pink region. The corresponding CIE chromaticity coordinates of ceramic samples are generally consistent at (0.61, 0.38), which all fall into the reddish-orange scope.

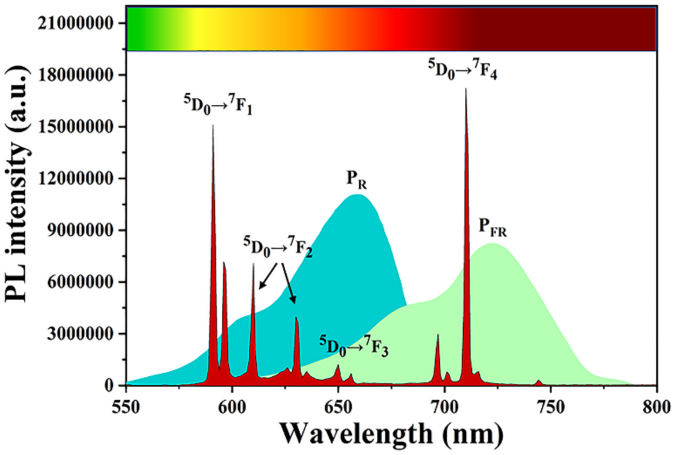

Fig. 6 Emission spectrum of the best $(Gd_{0.85}Lu_{0.1}Eu_{0.05})_3Al_5O_{12}$ ceramic composition together with the absorption spectra of phytochrome P_R and P_{FR}.

For the purpose of exploring the applicability for plant culture, we compare the PL spectrum of the best $(Gd_{0.85}Lu_{0.1}Eu_{0.05})_3Al_5O_{12}$ ceramic composition with the absorption spectra of phytochrome P_R and P_{FR} as shown in Fig. 6. The dominate far-red emission peak at ~710 nm from $^5D_0 \rightarrow ^7F_4$ transition of Eu^{3+} has a significant overlap with the absorption of phytochrome P_{FR}. This $^5D_0 \rightarrow ^7F_4$ emission peak position is quite analogous to those of previously reported Mn^{4+} activated $CaGdAlO_4$, $La(MgTi)_{1/2}O_3$, and $Ca_3La_2W_2O_{12}$ phosphor particles developed for plant cultivation [12,53,54]. On the other hand, the contributions of $^5D_0 \rightarrow ^7F_{1,2,3}$ emissions are relatively small to phytochrome P_R, because either their band intensities are weak or their peak positions are far away from the maximal absorption wavelength of phytochrome P_R. However, the second strongest luminescence band from

$^5D_0 \rightarrow ^7F_1$ transition of Eu^{3+} appears yellow emission. Yang *et al*. found that the yellow light was optimal for the growth and accumulation of bioactive flavonoids in some plants compared with white, red, or blue light [55]. In consequence, our developed ceramic phosphor could sufficiently provide both far-red and yellow emissions, implying the application potential to modulate plant growth as artificial light source.

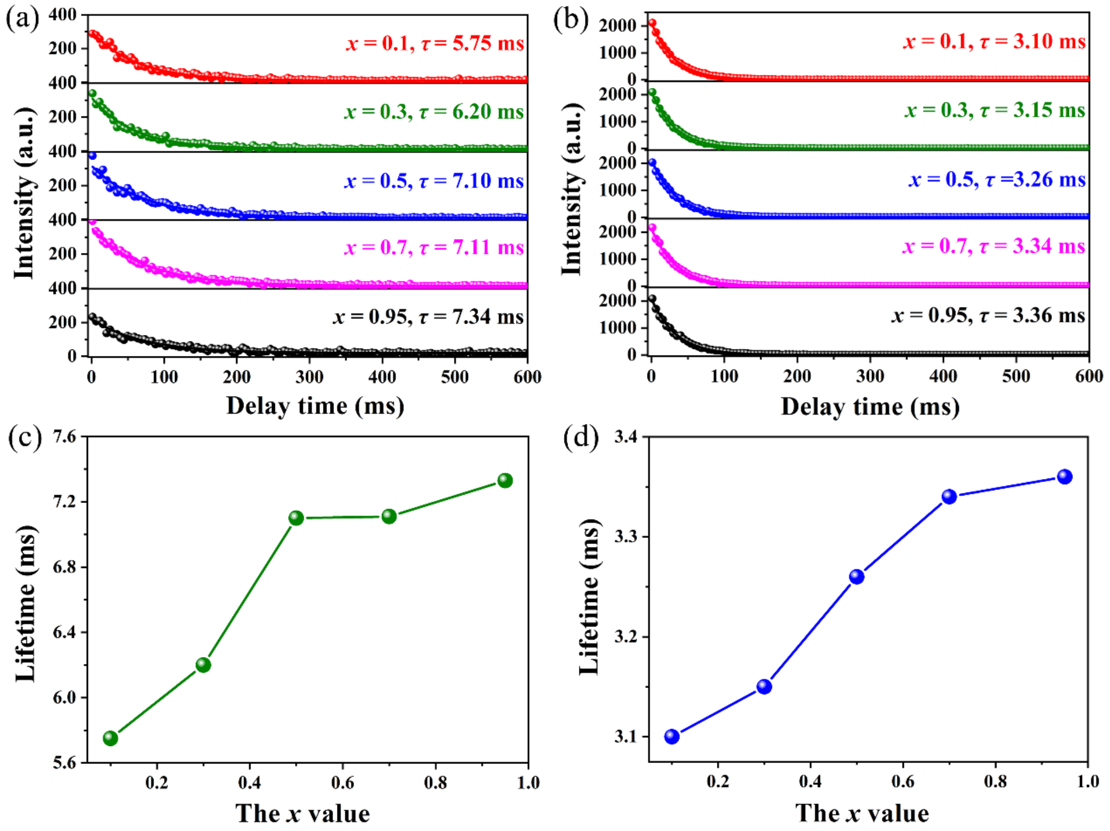

Fig. 7 Fluorescence decay kinetics of $(Gd_{0.95-x}Lu_xEu_{0.05})_3Al_5O_{12}$ (x = 0.1−0.95) phosphor particles (a) and ceramics (b) for 710 nm emission under 394 nm excitation of Eu^{3+}. Panels (c) and (d) show the relationships between lifetimes and x values for the powders and ceramics, respectively.

Figures 7(a) and (b) display the fluorescence decay kinetics of $(Gd_{0.95-x}Lu_xEu_{0.05})_3Al_5O_{12}$ (x = 0.1−0.95) particle and ceramic phosphors for 710 nm emission under 394 nm excitation of Eu^{3+}. The fluorescence lifetime can be deduced by fitting the decay curve with a single exponential model equation: $I=A\exp(-t/\tau)+B$, where I is the instantaneous fluorescence intensity, τ is the lifetime, t is the decay time, and *A* and *B* are constants [56-58]. The determined τ, *A*, and *B* parameters are listed in Table S2 of the supplementary material. The lifetime values vary from ~5.75 to 7.34 ms for particle phosphors while from ~3.10 to 3.36 ms for ceramic phosphors. The bulk samples have much shorter lifetimes than the particle counterparts due to the elimination of electron-attracting defects via improved crystallinity and grown grain [49,59]. It also can be seen that the lifetimes increase with the rising Lu^{3+} contents for both the two materials [Figs. 7(c) and (d)]. This is because Lu^{3+} addition significantly suppresses mass diffusion and crystallite/grain growth during particle calcination and ceramic sintering.

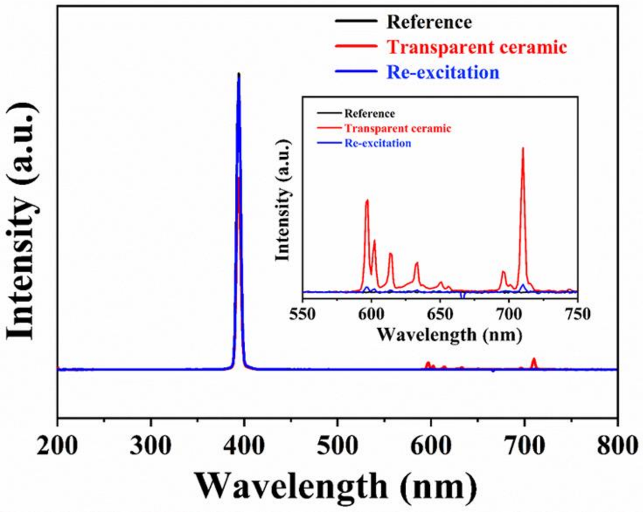

Fig. 8 Quantum efficiency measurement for the optimum composition of $(Gd_{0.85}Lu_{0.1}Eu_{0.05})_3Al_5O_{12}$ under 394 nm excitation. The inset is the enlargement for the wavelength range of Eu^{3+} emission.

Figure 8 depicts the response of the optimum ceramic composition of $(Gd_{0.85}Lu_{0.1}Eu_{0.05})_3Al_5O_{12}$ to the 394 nm excitation wavelength using solid barium sulfate white standard as a reference material. The quantum efficiency (η_{QE}) data are collected by an integrating sphere, which could be automatically derived according to Eq. (8) by a built-in software in the spectrophotometer [53,60].

$$\eta_{QE} = \frac{\int L_S}{\int E_R - \int E_S} \times 100\% \qquad (8)$$

where L_S stands for the emission spectrum of the specimen, and E_R and E_S represent the excitation spectra for the $BaSO_4$ reference material and the ceramic sample, respectively. The resulting quantum efficiency value for our transparent $(Gd_{0.85}Lu_{0.1}Eu_{0.05})_3Al_5O_{12}$ ceramic phosphor is ~42%, which is higher than the other Eu^{3+} doped aluminate garnet phosphors such as $Lu_3Al_5O_{12}$:Eu (~40%) and $Y_3Al_5O_{12}$:Eu (~40.5%) [61,62].

3.5 Thermal stability of luminescence for the transparent ceramic phosphor

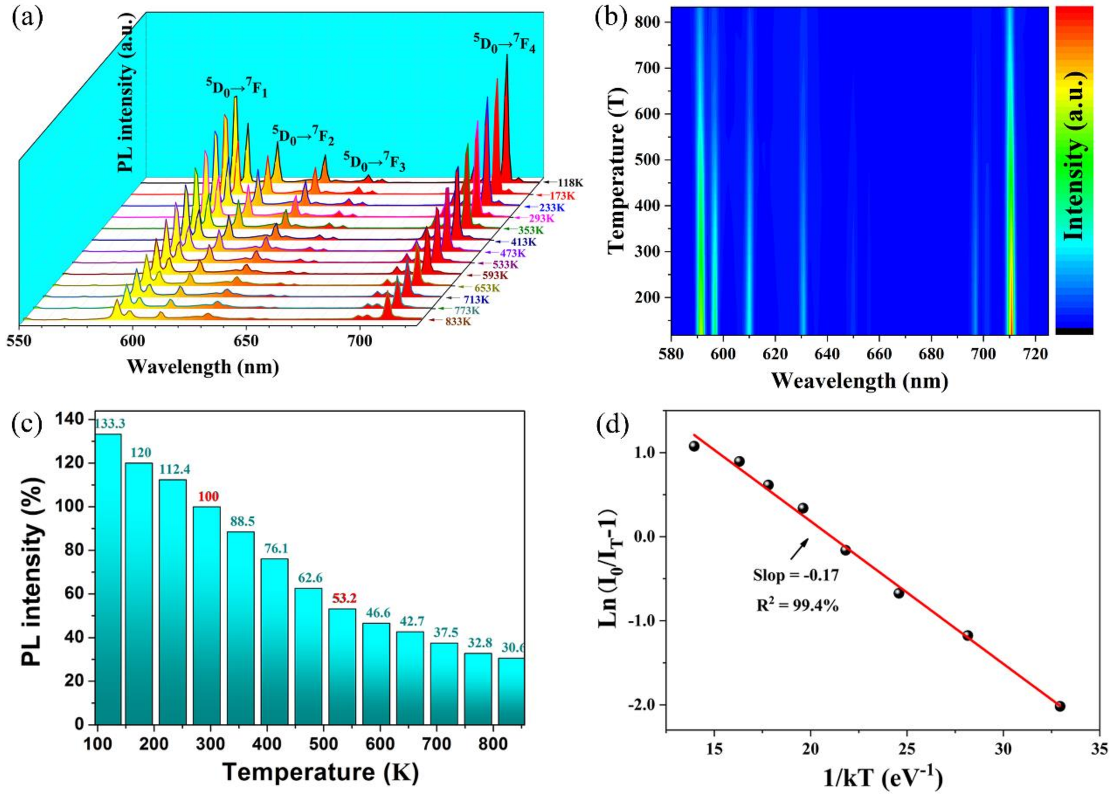

Fig. 9 The temperature-dependent PL spectra (a), the two-dimension plot of emission dependence on temperature (b), the normalized emission intensity (c), and the plot of $1/kT$ versus $\mathrm{Ln}(I_0/I_T\text{-}1)$ (d) of our best ceramic composition under 394 nm excitation.

The luminescent thermal stability is a significant parameter for the realized functionalization of fluorescent materials in solid-state lighting. The temperature-dependent luminescence measurement for the best fluorescent ceramic composition $(Gd_{0.85}Lu_{0.1}Eu_{0.05})_3Al_5O_{12}$ is performed in the temperature range of 118−833 K, and the results are shown in Figs. 9(a) and (b). With the increasing heating temperature, the PL intensity follows a trend of decline due to the thermal quenching effect derived from electron-phonon interaction. Moreover, the change in emission wavelength, if any, is only ~1 nm within the allowable system error (Fig. S7 in the supplementary material). If we assume the fluorescence intensity at room temperature to be 100%, the maximum value achieves at 118 K [Fig. 9(c)], which is ~1.33 times that of room temperature. The thermal quenching temperature, defined as the temperature at which PL intensity is 50% of the value at room temperature, is a little higher than 533 K for our sample. Such a high thermal quenching temperature indicates that our developed material has a high thermal stability of luminescence. The thermal stability of the sample is further evaluated by the activation energy of thermal quenching process based on Arrhenius equation (Eq. 9):

$$I_T = \frac{I_0}{1 + A\exp(-\Delta E / kT)} \tag{6}$$

where I_0 is the luminescence intensity at room temperature, I_T is the emission intensity at a certain temperature, k is Boltzmann constant (8.6×10^{-5} eV/K), A is a constant, and ΔE is the activation energy of thermal quenching [24,63,64]. The ΔE value can be estimated by taking the logarithm on both sides of this equation, *viz*., the plot of $Ln(I_0/I_T-1)$ against $(kT)^{-1}$ yields a straight line whose slope is equal to $-\Delta E$. As shown in Fig. 9(d), the resulting ΔE value is ~0.17 eV with a high degree of fitting (R^2 = 99.4%), which is equivalent to the commercially available $Y_2O_3:Eu^{3+}$ red phosphor (0.17 eV) [65]. The probability of a nonradiative transition per unit time (α) is closely associated with the activation energy according to Eq. (10):

$$\alpha = s\exp(\frac{-\Delta E}{kT}) \tag{10}$$

where s is the frequency factor [66]. Apparently, a high activation energy would effectively suppress the probability of nonradiative transition.

3.6 EL properties of the designed LED lamp

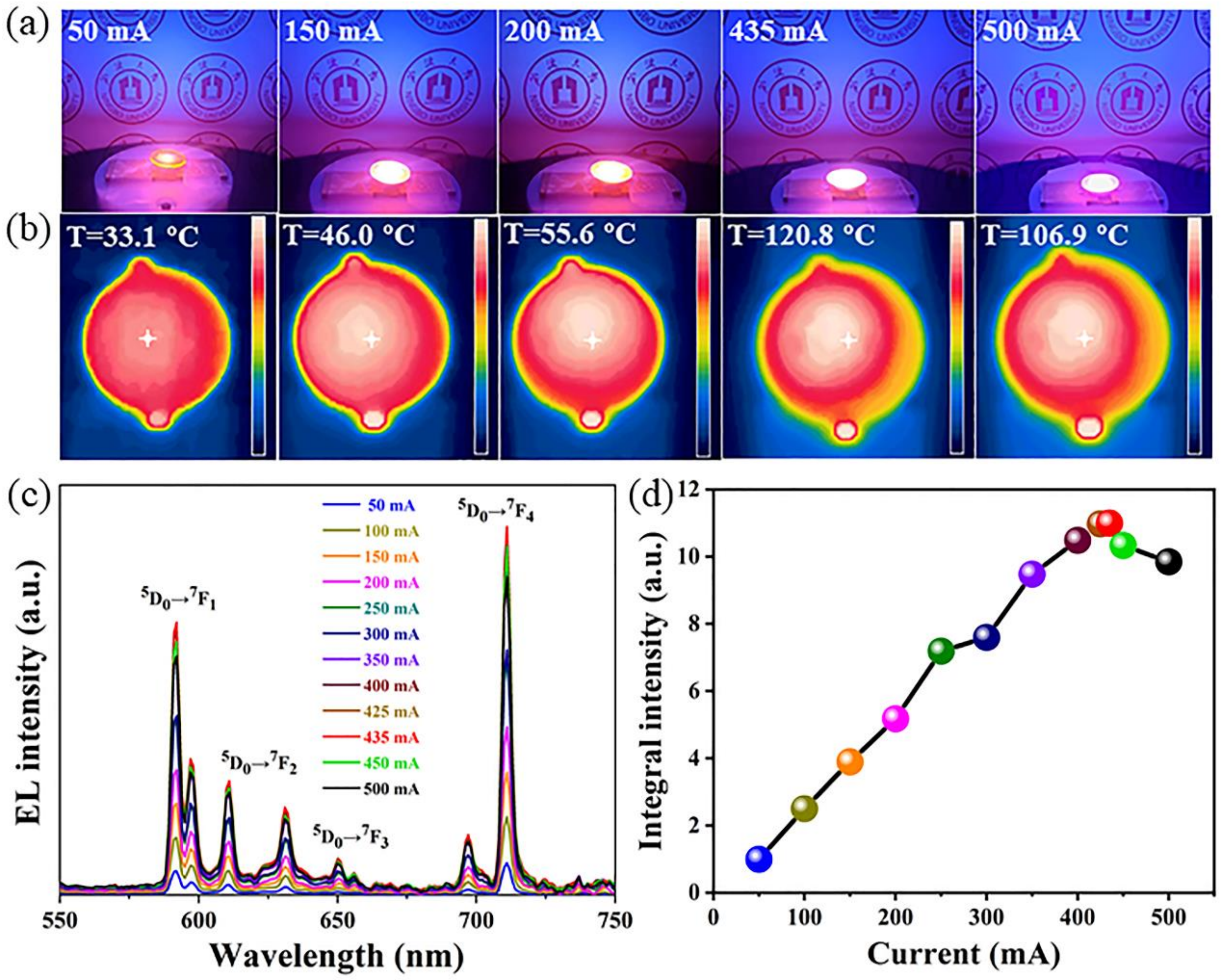

Fig. 10 Appearance photographs (a), thermal radiation images (b), EL emission spectra (c), and EL integral intensities normalized to 1 (d) of the prepared LED lamp at working currents of 50−500 mA.

The best fluorescent ceramic specimen is directly covered on a near UV (390−395 nm) chip to package a LED device without any organic polymers and its appearance can be seen from Fig. S8 of the supplementary material. Under an injection current of 50 mA, the assembled LED lamp emits weak red emission as shown in Fig. 10(a). Applying a higher working current of more than 150 mA yields the strong glaring red emission. As the current increases, the junction temperature of the packaged red-emitting LED shows an increasing tendency up to maximum of ~120.8 ºC at 435 mA, and then decreases to ~106.9 ºC at 500 mA. Compared with particle phosphor converted LED [67], our ceramic phosphor converted LED exhibits a lower junction temperature and a more uniform thermal radiation at each current due to its higher conductivity via avoiding using the organic polymer and its own feature of pure substance. As presented in Fig. 10(c), the EL emission spectra also display the characteristic $^5D_0 \rightarrow {}^7F_J$ ($J = 1-4$) transition of Eu^{3+} and their intensities rise with enhanced injection current up to 435 mA, and then decrease at a higher current. That is, the 435 mA current seems to be the saturation point. Such a phenomenon may be attributed to the induced thermal effect referred to Fig. 10(b). From the normalized curve [Fig. 10(d)], the EL integral intensity at 435 mA is ~11-fold higher than that at 50 mA. At this saturation current, the corresponding color coordinates, color rendering index (CRI), and correlated color temperature (CCT) are (0.61, 0.39), 81.6, and 1745 K, respectively. The elevated working current increases the CRI parameter, but has little effect on CCT and color coordinates (Table S3 in the supplementary material). The phenomenon of saturated injection current for electroluminescence has seldom studied for comparison. However, we believe that the pore-free ceramics may have a higher saturated value relative to the powder forms and the translucent ceramics due to the higher thermal conductivity.

4 Conclusions

A series of $(Gd_{0.95-x}Lu_xEu_{0.05})_3Al_5O_{12}$ ($x = 0.1-0.95$) particle and ceramic phosphors were prepared to study the compositional effects on structure features, sintering behaviors, and luminescence properties. All the phosphors exhibit main far-red emission at ~710 nm arising from $^5D_0 \rightarrow {}^7F_4$ transition, which overlaps with the absorption of phytochrome P_{FR}. A Lu^{3+} dopant increases the theoretical density, suppresses the crystallite/grain growth, reduces the luminescence intensity, and delays the fluorescence lifetime. The optimum $x = 0.1$ ceramic composition exhibits optical grade with near-zero optical loss, a high quantum efficiency of ~42%, and excellent thermal stability with an activation energy of ~0.17 eV. The designed ceramic phosphor converted LED possesses a saturation injection current of 435 mA, high color rendering index of 81.6, and low correlated color temperature of 1745 K. Our findings suggest that the developed red-emitting LED has potential application for plant cultivation.

Acknowledgment

The research was supported by Zhejiang Provincial Natural Science Foundation of China under Grant No. LY23F050007.

Declaration of competing interest

The authors have no competing interests to declare that are relevant to the content of this article.

Appendix A. Supplementary data

Supplementary data to this article can be found in the “Supplementary Material” section.

References

[1] Nagano S, Guan KL, Shenkutie SM, *et al.* Structural insights into photoactivation and signalling in plant phytochromes. *Nat Plants* 2020, **6**: 581–588.

[2] Li L, Cao QW, Xie J, *et al*. Novel far-red emitting phosphor Mn^{4+}-activated $BaLaLiWO_6$ with excellent performance for indoor plant cultivation of light-emitting diodes. *J Alloys Compd* 2023, **934**: 167927.

[3] Yan ZW, Yang XL, Xiao SG. Far-red-emitting $Li_6SrLa_2Sb_2O_{12}$: Mn^{4+} phosphor for plant growth LEDs application. *Mater Res Bull* 2021, **133**: 111040.

[4] Li G, Liu GG, Mao QN, *et al*. Novel non-rare-earth red-emitting phosphor Li_4AlSbO_6:Mn^{4+} for plant growth: Crystal structure, luminescence properties and its LED device. *Ceram Int* 2021, **47**: 27609–27616.

[5] Gao PX, Zhou ZY, Dong P, *et al*. Tuning the luminescence properties of blue and far-red dual emitting Gd_2MgTiO_6:Bi^{3+},Cr^{3+} phosphor for LED plant lamp. *J Am Ceram Soc* 2021, **104**: 6444–6454.

[6] Smith H. Phytochromes and light signal perception by plants—an emerging synthesis. *Nat* 2000, **407**: 585–591.

[7] Ince YC, Krahmer J, Fiorucci A-S, *et al*. A combination of plasma membrane sterol biosynthesis and autophagy is required for shade-induced hypocotyl elongation. *Nat Commun* 2022, **13**: 5659.

[8] Cheng K, Xu YM, Liu XY, *et al*. A novel far-red phosphors $Li_2ZnTi_3O_8$:Cr^{3+} for indoor plant cultivation: Synthesis and luminescence properties. *Ceram Int* 2023, **49**: 6343–6350.

[9] Wang XJ, Feng XW, Molokeev MS, *et al*. Broadband green to broadband deep red modulation of Bi^{3+} luminescence in Lu_2WO_6 by Gd^{3+} doping and application in high color rendering index white LED and near-infrared LED. *Dalton Trans* 2023, **52**: 2619–2630.

[10] Zhu QQ, Li SX, Yuan Q, *et al*. Transparent YAG:Ce ceramic with designed low light scattering for high-power blue LED and LD applications. *J Eur Ceram Soc* 2021, **41**, 735–740.

[11] Xue BW, Hu LB, Xiong PX, *et al*. Effects of activator oxidation number and matrix composition on structure feature, microscopic morphology, and luminescence behavior of blue-emitting (Gd,Y)$_3$Al$_5$O$_{12}$:Bi phosphors. *J Lumin* 2023, **257**: 119737.

[12] Huang XY, Guo H. Finding a novel highly efficient Mn^{4+}-activated Ca$_3$La$_2$W$_2$O$_{12}$ far-red emitting phosphor with excellent responsiveness to phytochrome P$_{FR}$: Towards indoor plant cultivation application. *Dyes Pigments* 2018, **152**: 36–42.

[13] Tarala VA, Kravtsov AA, Malyavin FF, *et al*. Optical properties of non-stoichiometric YAG:Ce luminescent ceramics. *Opt Mater* 2023, **143**: 114231.

[14] Zhang YZ, Lei CX, Fu Q. Fully organic bulk polymer with metallic thermal conductivity and tunable thermal pathways. *Adv Sci* 2021, **8**: 2004821.

[15] Kwon SB, Yoo JH, Choi SH, *et al*. Preparation of high-quality YAG:Ce^{3+} ceramic phosphor by high-frequency induction heated press sintering methods. *Sci Rep* 2022, **12**: 20477.

[16] Upasani M, Butey B, Moharil SV. Synthesis, characterization and optical properties of Y$_3$Al$_5$O$_{12}$:Ce phosphor by mixed fuel combustion synthesis. *J Alloys Compd* 2015, **650**: 858–862.

[17] Wang MY, Lu B. Manufacture and Faraday magneto-optical effect of highly transparent novel holmium aluminum garnet ceramics. *Scr Mater* 2021, **195**: 113729.

[18] Ratzker B, Wagner A, Kalabukhov S, *et al*. Controlled pore growth for enhanced photoluminescence of ceramic phosphors. *Scr Mater* 2021, **202**: 114008.

[19] Ling JR, Zhang Y, Yang J, *et al*. A single-structured LuAG:Ce,Mn phosphor ceramics with high CRI for high-power white LEDs. *J Am Ceram Soc* 2022, **105**: 5738–5750.

[20] Jain A, Koyani R, Munoz C, *et al*. Magnetic-luminescent cerium-doped gadolinium aluminum garnet nanoparticles for simultaneous imaging and photodynamic therapy of cancer cells. *J Colloid Interface Sci* 2018, **526**: 220–229.

[21] Li J-G, Sakka Y. Recent progress in advanced optical materials based on gadolinium aluminate garnet (Gd$_3$Al$_5$O$_{12}$). *Sci Technol Adv Mater* 2015, **16**: 014902.

[22] Oh HM, Kim HN, Park YJ, *et al*. Optical properties and laser performance of Nd:Y_2O_3 ceramics with fine-grained microstructure. *J Eur Ceram Soc* 2021, **41**: 4419−4423.

[23] Pokorny M, Babin V, Beitlerova A, *et al*. Gd-admixed (Lu,Gd)AlO_3 single crystals: breakthrough in heavy perovskite scintillators. *NPG Asia Mater* 2021, **13**: 66.

[24] Xiang Y, Liu ZY, Gao Y, *et al*. Novel double perovskite $Ca_2Gd_{0.5}Nb_{1-x}W_{5x/6}O_6$:0.5$Eu^{3+}$ red phosphors with excellent thermal stability and high color purity for white LEDs. *Chem Eng J* 2023, **456**: 140901.

[25] Wang XY, Lu B, Xia HP. Novel red-emitting orthorhombic $GdInO_3$:Eu^{3+} perovskite phosphor: Structural resolution, Judd-Ofelt theory, and comparative investigation with hexagonal counterpart. *Mater Today Nano* 2023, **21**: 100291.

[26] Wu ZD, Ai SH, Chen H, *et al*. Sol-gel synthesized double perovskite $Na_{(1-x)}Gd_{(0.95+x/3)}MgWO_6$:5% Eu^{3+} ($0 \leq x \leq 0.5$) phosphors with incommensurately modulated structure: Microstructures and luminescence properties. *Opt Laser Technol* 2022, **150**: 107947.

[27] Xu J, Wan R, Xu W, *et al*. Colored radiative cooling coatings using phosphor dyes. *Mater Today Nano* 2022, **19**: 100239.

[28] Miao SH, Shi RQ, Zhang Y, *et al*. Deep-red $Ca_3Al_2Ge_3O_{12}$:Eu^{3+} garnet phosphor with near-unity internal quantum efficiency and high thermal stability for plant growth application. *Adv Mater Technol* 2023, **8**: 2202103.

[29] Su XB, Zhang K, Liu Q, *et al*. Combinatorial optimization of $(Lu_{1-x}Gd_x)_3Al_5O_{12}$:$Ce_{3y}$ yellow phosphors as precursors for ceramic scintillators. *ACS Comb Sci* 2011, **13**: 79–83.

[30] Li JK, Li J-G, Zhang ZJ, *et al*. Gadolinium aluminate garnet ($Gd_3Al_5O_{12}$): Crystal structure stabilization via lutetium doping and properties of the $(Gd_{1-x}Lu_x)_3Al_5O_{12}$ solid solutions (x = 0–0.5). *J Am Ceram Soc* 2012, **95**: 931–936.

[31] Zazubovich S, Laguta VV, Machek P, *et al*. Effect of Li^+ co-doping on the luminescence and defects creation processes in $Gd_3(Ga,Al)_5O_{12}$:Ce scintillation crystals. *J Lumin* 2022, **242**: 118548.

[32] Perdew JP, Burke K, Ernzerhof M. Generalized gradient approximation made simple. *Phys Rev Lett* 1996, **77**: 3865–3868.

[33] Bartel CJ, Millican SL, Deml AM, *et al*. Physical descriptor for the Gibbs energy of inorganic crystalline solids and temperature-dependent materials chemistry. *Nat Commun* 2018, **9**: 4168.

[34] Wang XY, Lu B, Feng K, *et al*. Vacuum sintering of novel transparent Tm_2O_3 ceramics: Effect of silica additive and thermal performance. *J Eur Ceram Soc* 2020, **41**: 6249–6253.

[35] Hu LB, Lu B, Xue BW, *et al*. Production and characterization of highly transparent novel magneto-optical $Ho_2Zr_2O_7$ ceramics with anion-deficient fluorite structures. *J Mater Sci Techno* 2023, **150**: 217–224.

[36] Wang MY, Lu B, Li HX. Fantastic valence impacts of Pr on microstructures and Faraday magneto-optical effects of transparent $(Ho,Pr)_2O_3$ ceramics. *J Eur Ceram Soc* 2021, **41**: 5258–5263.

[37] Chen PH, Li XY, Tian F, *et al*. Fabrication, microstructure, and properties of 8 mol% yttria-stabilized zirconia (8YSZ) transparent ceramics. *J Adv Ceram* 2022, **11**: 1153–1162.

[38] Xiong YF, Shi Y, Wang HB, *et al*. Ce^{3+}, Pr^{3+} co-doped $Lu_3Al_5O_{12}$ single crystals and ceramics: A comparative study. *Materials* 2022, **15**: 9025.

[39] Sugiyama M, Fujimoto Y, Yanagida T, *et al*. Crystal growth and scintillation properties of Er-doped $Lu_3Al_5O_{12}$ single crystals. *Nucl Instrum Methods Phys Res A* 2012, **664**: 127–131.

[40] Lu B, Wu SF, Cheng HM, *et al*. Binary transparent $(Ho_{1-x}Dy_x)_2O_3$ ceramics: Compositional influences on particle properties, sintering kinetics and Faraday magneto-optical effects. *J Eur Ceram Soc* 2021, **41**: 2826–2833.

[41] Kimmel G, Sahartov A, Sadia Y, *et al*. Non-monotonic lattice parameters variation with crystal size in nanocrystalline CeO_2. *J Mater Res Technol* 2021, **12**: 87–99.

[42] Yang H, Wang ZC, Song LZ, *et al*. A study on the coercivity and the magnetic anisotropy of the lithium ferrite nanocrystallite. *J Phys D: Appl Phys* 1996, **29**: 2574–2578.

[43] Li XD, Li J-G, Xiu ZM, *et al*. Effects of Gd^{3+} substitution on the fabrication of transparent $(Y_{1-x}Gd_x)_3Al_5O_{12}$ ceramics. *J Am Ceram Soc* 2010, **93**: 2229–2235.

[44] Guo WA, Jiang BX, Zhu JJ, *et al*. Surface structure and electronic properties of $Lu_3Al_5O_{12}$. *Crystals* 2021, **11**: 1433.

[45] Shi Y, Shichalin O, Xiong YF, *et al*. Ce^{3+} doped $Lu_3Al_5O_{12}$ ceramics prepared by spark plasma sintering technology using micrometre powders: Microstructure, luminescence, and scintillation properties. *J Eur Ceram Soc* 2022, **41**: 6663–6670.

[46] Wang XY, Lu B. Influences of silica additive on sintering and Hall effect of novel transparent In_2O_3 semiconductive ceramics. *Scr Mater* 2021, **193**: 137–141.

[47] Cheng HM, Lu B, Liu YX, *et al*. Transparent magneto-optical Ho_2O_3 ceramics: Role of self-reactive resultant oxyfluoride additive and investigation of vacuum sintering kinetics. *Ceram Int* 2019, **45**: 14761–14767.

[48] Lai YQ, Lu B, Wang M. Optical properties and Faraday magneto-optical effects of highly transparent novel $Tb_2Zr_2O_7$ fluorite ceramics. *Scr Mater* 2023, **227**: 115282.

[49] Lu B, Li J-G, Suzuki TS, *et al*. Effects of Gd substitution on sintering and optical properties of highly transparent $(Y_{0.95-x}Gd_xEu_{0.05})_2O_3$ ceramics. *J Am Ceram Soc* 2015, **98**: 2480–2487.

[50] Wang XJ, Feng XW, Sun M, *et al*. Synthesis of multi-type rare earth compounds with $RE(OH)SO_4$ as a new sacrificial-template and photoluminescence. *J Asian Ceram Soc* 2022, **10**: 575–582.

[51] Souza AS, Oliveira YAR, Couto dos Santos MA. Enhanced approach to the Eu^{3+} ion $^5D_0\rightarrow{}^7F_0$ transition intensity. *Opt Mater* 2013, **35**: 1633–1635.

[52] Skaudzius R, Katelnikovas A, Enseling D, *et al*. Dependence of the $^5D_0\rightarrow{}^7F_4$ transitions of Eu^{3+} on the local environment in phosphates and garnets. *J Lumin* 2014, **147**: 290–294.

[53] Hu JX, Huang TH, Zhang YP, *et al*. Enhanced deep-red emission from Mn^{4+}/Mg^{2+} codoped $CaGdAlO_4$ phosphors for plant cultivation. *Dalton Trans* 2019, **48**: 2455–2466.

[54] Zhou ZW, Zheng JM, Shi R, *et al*. Ab initio site occupancy and far-red emission of Mn^{4+} in cubic-phase $La(MgTi)_{1/2}O_3$ for plant cultivation. *ACS Appl Mater Interfaces* 2017, **9**: 6177–6185.

[55] Yang QR, Pan JQ, Shen GA, *et al*. Yellow light promotes the growth and accumulation of bioactive flavonoids in Epimedium pseudowushanense. *J Photoch Photobio B* 2019, **197**: 111550.

[56] Li WL, Sun YF, Chen ZY, *et al*. Novel Sm^{3+} doped $BaZn_2(PO_4)_2$ glass-ceramic for optically stimulated luminescence dosimetry. *J Non-Cryst Solids* 2022, **594**: 121796.

[57] Ma CC, Wang MY, Xue BW, *et al*. Structural features and photoluminescence behaviors of color-temperature tunable $(Gd,Y)_3Al_5O_{12}$:Ce^{3+}/Cr^{3+} phosphors with varying compositions. *J Non-Cryst Solids* 2022, **588**: 121645.

[58] Feng K, Lu B, Hu LB. Down/upconversion luminescence behaviors and temperature-sensing properties of highly transparent $(Er_{1-x}Yb_x)_2O_3$ ceramics. *ACS Appl Electron Mater* 2022, **4**: 761–767.

[59] Lu B, Li J-G, Suzuki TS, *et al*. Controlled synthesis of layered rare-earth hydroxide nanosheets leading to highly transparent $(Y_{0.95}Eu_{0.05})_2O_3$ Ceramics. *J Am Ceram Soc* 2015, **98**: 1413–1422.

[60] Sun ZG, Chen ZY, Wang MY, *et al*. Production and optical properties of Ce^{3+}-activated and Lu^{3+}-stabilized transparent gadolinium aluminate garnet ceramics. *J Am Ceram Soc* 2020, **103**: 809–818.

[61] Uhlich D, Hupperta P, Wiechert DU, *et al*. Preparation and characterization of nanoscale lutetium aluminium garnet (LuAG) powders doped by Eu^{3+}. *Opt Mater* 2007, **29**: 1505–1509.

[62] Lu C-H, Huang C-H. Sensitized photoluminescence of Eu^{3+} and Gd^{3+}-doped $Y_3Al_5O_{12}$ phosphors prepared via a reverse microemulsion process. *Chem Lett* 2004, **12**: 1568–1569.

[63] Wang XJ, Feng XW, Gong CS, *et al*. $(La,Dy)_2W_2O_9$ tungstates: Selected synthesis, enhanced luminescence through Gd^{3+} co-doping, and favorable quantum efficiency. *Adv Powder Techno* 2022, **33**: 103392.

[64] Yu B, Li C, Wang YJ, *et al*. A new eulytite-type $Pb_3Bi(PO_4)_3$:Eu^{3+} red-emitting phosphor: Synthesis, structure and photoluminescence characteristics. *J Lumin* 2020, **220**: 1169.

[65] Fhoula M, Dammak M. Optical spectroscopy and Judd-Ofelt analysis of Eu^{3+} doped in $Na_2ZnP_2O_7$ with high thermal stability for display applications. *J Lumin* 2020, **223**: 117–193.

[66] Zheng CZ, Xiong PX, Peng MY, *et al*. Discovery of a novel rare-earth free narrow-band blue-emitting phosphor $Y_3Al_2Ga_3O_{12}:Bi^{3+}$ with strong NUV excitation for LCD LED backlights. *J Mater Chem C* 2020, **8**: 13668–13675.

[67] Zhong YQ, Zeng QF, Qian XQ, *et al*. Designing multicolor luminescence in Tb^{3+}/Eu^{3+}-codoped KGd_2F_7 nanoparticles through energy transfer engineering for warm white light-emitting diode. *J Lumin* 2023, **261**: 119916.

Figure captions

Fig. 1 XRD patterns of the target particle products for $(Gd_{0.95-x}Lu_xEu_{0.05})_3Al_5O_{12}$ (x = 0.1−0.95) obtained by calcining the precursors at 1200 ºC for 4 h (a) and the corresponding bulk materials fabricated by vacuum sintering (b). The two insets in the right-hand panels show the enlarged view of the main (420) diffraction peak.

Fig. 2 Lattice constants and theoretical densities of $(Gd_{0.95-x}Lu_xEu_{0.05})_3Al_5O_{12}$ powders (a) and ceramics (b) as a function of x value.

Fig. 3 Appearances (a) and in-line transmittances (b) of transparent $(Gd_{0.95-x}Lu_xEu_{0.05})_3Al_5O_{12}$ (x = 0.1−0.95) ceramics. The lower part in panel (a) shows the red emission of $(Gd,Lu)_3Al_5O_{12}$:Eu ceramics irradiated by a 365 nm ultraviolet lamp. The embedded image in panel (b) displays the thermal etching polished surface of the best specimen with $x = 0.1$. The samples are all ~1.0 mm in thickness.

Fig. 4 D-SEM micrographs showing the surface microstructures of vacuum sintered $(Gd_{0.95-x}Lu_xEu_{0.05})_3Al_5O_{12}$ specimens with $x = 0.1$ (a) and 0.95 (b).

Fig. 5 PLE (a, c) / PL spectra (b, d) and CIE chromaticity diagrams (e, f) of $(Gd_{0.95-x}Lu_xEu_{0.05})_3Al_5O_{12}$ powders (a, c, e) and ceramics (b, d, f) as a function of x value.

Fig. 6 Emission spectrum of the best $(Gd_{0.85}Lu_{0.1}Eu_{0.05})_3Al_5O_{12}$ ceramic composition together with the absorption spectra of phytochrome P_R and P_{FR}.

Fig. 7 Fluorescence decay kinetics of $(Gd_{0.95-x}Lu_xEu_{0.05})_3Al_5O_{12}$ (x = 0.1−0.95) phosphor particles (a) and ceramics (b) for 710 nm emission under 394 nm excitation of Eu^{3+}. Panels (c) and (d) show the relationships between lifetimes and x values for the powders and ceramics, respectively.

Fig. 8 Quantum efficiency measurement for the optimum composition of $(Gd_{0.85}Lu_{0.1}Eu_{0.05})_3Al_5O_{12}$ under 394 nm excitation. The inset is the enlargement for the wavelength range of Eu^{3+} emission.

Fig. 9 The temperature-dependent PL spectra (a), the two-dimension plot of emission dependence on temperature (b), the normalized emission intensity (c), and the plot of $1/kT$ versus $\mathrm{Ln}(I_0/I_T\text{-}1)$ (d) of our best ceramic composition under 394 nm excitation.

Fig. 10 Appearance photographs (a), thermal radiation images (b), EL emission spectra (c), and EL integral intensities normalized to 1 (d) of the prepared LED lamp at working currents of 50−500 mA.